# Development of solar arrays for Argentine satellite missions

M. Alurralde [a], M. Barrera [a,b], C.G. Bolzi [a], C.J. Bruno [a], P. Cabot [c], E. Carella [c], J. Di Santo [a], J.C. Durán [a,*], D. Fernández Slezak [a], J. Fernández Vázquez [a], A. Filevich [a], C.D. Franciulli [a], J.A. García [a,1], E.M. Godfrin [a], L. González [a], V. Goldbeck [d], A. Iglesias [e], M.G. Martínez Bogado [a,b], E. Mezzabolta [a], A. Moglioni [c], S. Muñoz [a], C. Nigri [a,1], S.L. Nigro [a], J.I. Pérez [a], J. Plá [a,b], I. Prario [a,1], M.C. Raffo Calderón [e], D. Raggio [a], C. Rinaldi [a], S.E. Rodríguez [a], H. Socolovsky [a,1], M.J.L. Tamasi [a,b]

[a] Gerencia Investigación y Aplicaciones, CAC, CNEA, Av. General Paz 1499, 1650 San Martín, Provincia de Buenos Aires, Argentina
[b] Consejo Nacional de Investigaciones Científicas y Técnicas (CONICET), Argentina
[c] Departamento Ensayos No Destructivos y Estructurales, CAC, CNEA, Argentina
[d] Departamento Materiales, CAC, CNEA, Argentina
[e] Gerencia Química, CAC, CNEA, Argentina

## ARTICLE INFO

## ABSTRACT

This paper presents the development of solar arrays for Argentine satellite missions performed within the frame of cooperation agreements between the Argentine National Atomic Energy Commission (CNEA) and the Argentine National Commission for Space Activities (CONAE). Relevant issues such as simulation and design, solar cells characterisation, set up of soldering and bonding processes, radiation damage and development of testing techniques, are reviewed. A chamber for testing solar cells and other devices in a simulated space environment, and the integration and tests of two engineering models for qualification of space technology processes are described. The requirements and solar array design for 3 missions, Aquarius/SAC-D and SAOCOM 1A and 1B, are presented. Finally, the flight model for the SAC-D mission, which was launched on 10 June 2011, is outlined, and telemetry data analysis from the first stages of the mission is presented.

## 1. Introduction

By the end of 1995, the Solar Energy Department (DES) of the National Atomic Energy Commission (CNEA) began activities related with solar cells and solar arrays for space applications. To this end, CNEA and the National Commission for Space Activities (CONAE) signed a cooperation agreement which led to a first experiment: Argentine Solar Cells in Space, on board of the Argentine satellite SAC-A (Satellite for Scientific Applications – A) launched by the end of 1998 [9].

After this experiment, CNEA and CONAE signed new cooperation agreements for the development of the solar arrays for three Argentine missions:

– SAOCOM 1A and 1B missions for Earth observation. These satellites are part of a future constellation, SIASGE [22], planned for monitoring natural and man-made disasters, as

well as harvests, natural resources, and soil moisture. This project is a joint venture with the Italian Space Agency (ASI).

– Aquarius/SAC-D mission, for scientific research and Earth observation. CONAE and the USA National Aeronautics and Space Administration, NASA, have jointly developed the SAC-D/Aquarius [21]. The scientific objective is to conduct observations of the Earth in order to obtain new information on climate by measuring sea surface salinity. SAC-D must also identify hot spots on the ground surface to allow the mapping of fire risk, and perform measurements of soil humidity to prevent floodings (early warning).

In this paper we describe the development of the technologies for the integration and testing of solar arrays for space applications. Particularly, the integration and testing of two engineering models are shown. It should be remarked that NASA and ESA (European Space Agency) documents [23,28] have been taken as references for these developments.

The main activities performed on flight components were carried out in a clean room – Class 10,000 (according to FED-STD-209D), shown in Fig. 1. Other development work has been carried out in different facilities belonging to the Tandar Accelerator Laboratory, CNEA.

* Corresponding author.
  *E-mail address:* duran@tandar.cnea.gov.ar (J.C. Durán).
[1] PhD student.

**Fig. 1.** Solar Array Integration Laboratory, clean room – Class 10,000.

Further activities related with simulation and characterisation of III–V solar cells, beyond the scope of this paper, are presented elsewhere [7,26].

## 2. Solar array design and simulation

A solar array is composed by strings of solar cells connected in series. The number of cells in each string depends on the operating voltage required. Strings are connected in parallel conforming modules, which are the commutable units handled by the regulator.

The sizing of a solar array for satellite missions can be achieved by means of theoretical simulations of the power subsystems, taking into account the mission's requirements and, in a detailed way, the consumption profile of the satellite. To this end two models and their corresponding computational codes have been developed.

The first code allows classifying the cells and calculates the total current–voltage ($I$–$V$) curve of a solar array by adding numerically (in series or in parallel) the $I$–$V$ curves of each component (solar cells, diodes, wires, etc.). Unlike usual models [8,10, 14,25] which use theoretical equations for the simulation of the $I$–$V$ curve of the cells and do not take into account the deviation in the electrical characteristics of the cells, this code does not require any model for the electrical characteristics, only a set of $I$–$V$ values defining the curve for each component. If available it may use the actual (measured) $I$–$V$ curves of the solar cells that will be integrated into the solar panel, or theoretical values randomly generated using mean values and standard deviations provided by the solar cells manufacturer. The code allows to classify the cells by: short circuit current ($I_{sc}$), voltage at maximum power point ($V_{mpp}$), maximum power point ($P_{mpp}$), open circuit voltage ($V_{oc}$), current at maximum power point ($I_{mpp}$), or current at a fixed voltage ($I_{fv}$).

The second code simulates the power subsystem, which consists of a solar array, batteries, and regulator. The aim of the simulation code is to obtain the temporal evolution of several important parameters during the mission's (beginning of life (BOL), end of life (EOL) or at intermediate states). At each step (time = $t$), the code takes into account the intensity of the solar radiation and the satellite position, calculates the solar radiation incidence angle and generates the array $I$–$V$ curve. Then, using the satellite consumption and the state of charge of the battery at $t$, the subroutine

which simulates the regulator defines the number of modules of the solar array that should be on (part of the modules may be short-circuited to avoid overcharge of the batteries). Finally, the current provided by the solar array and the batteries, and the new state of charge of the battery at ($t + \Delta t$) are calculated. The simulation is performed with a typical time step of 1 minute.

The main input information for the simulation code is:

(i) $I$–$V$ curves of modules, previously calculated for normal incidence at several operating temperatures;
(ii) charge and discharge curves of batteries for several operating temperatures;
(iii) regulator thresholds;
(iv) the consumption profile;
(v) orbit information (type, altitude, inclination, eclipses duration, etc.).

Factors associated with radiation damage, incidence angle, Sun–Earth distance and operation temperature are considered.

The simulation code was written in Fortran 90, using an object-oriented design.

The models developed have been applied for designing the solar arrays and predicting the power subsystems performance for SAOCOM and SAC-D missions. Energy needs for the satellites and available solar array area led to choose InGaP/GaAs/Ge advanced triple junction (ATJ) solar cells from Emcore [16], with a minimum average efficiency of 27.5% (28 °C, AM0), and an area of 27.5 cm$^2$.

### 2.1. SAOCOM mission

The SAOCOM 1A satellite will describe a Sun-synchronous frozen orbit at approximately 620 km height, with an inclination of 98° and an orbital hour LTAN 6:12 AM. The orbital period will be 98 minutes, with variable eclipse periods during 4 months each year at northern latitudes, and a maximum duration of 19 minutes on December. For the solar array parallel to the orbit plane (normal mode of operation), the angle of incidence of the solar radiation on the solar cells will vary between 31° (December), 15° (June) and 4° (March and September).

The main instrument of the satellite will be an approximately 35 m$^2$ radar antenna. The high power requirement of the satellite is associated to the operation of this antenna and also with manoeuvres of the satellite (rotations) for observation at different

directions. The satellite will have a base consumption of about 1.4 kW and a maximum consumption of approximately 4.9 kW during antenna operations. The mean power requirement will strongly depend on the number of observations per day and the duration of each observation. The available area for the solar array is approximately 13 m$^2$ and the battery will be composed of Li-ion cells with a nominal voltage of 50 V and a capacity of 128 Ah at EOL. The maximum depth of discharge (DOD) has been recommended not to exceed 20% to optimise the battery lifetime.

For the design and simulation presented below, the following mission requirement has been considered:

- The power generation at EOL (5 years) shall be of at least 1900 W orbital mean value with one generation module failed, and during worst-case illumination condition.

The solar array will be integrated with ATJ solar cells, each one bridged by a silicon bypass diode, provided by Emcore. The solar cells will be interconnected in strings with one blocking diode in each string. The number of cells per string is determined by the operating voltage defined by the battery. Assuming a mean state of charge (SOC) of 90%, which defines an operating voltage of 61.4 V, and taking into account the electrical characteristics of the solar cells, the number of cells interconnected in series for each string should be 32.

Using the code for the interconnection of cells and the cell curves obtained from the electrical parameters ($I_{sc}$, $V_{oc}$, $I_{mpp}$ and $V_{mpp}$) of 2700 solar cells at 28 °C (data supplied by the manufacturer) as input, the $I$–$V$ curves of the modules were generated for the following operating conditions:

(i) EOL (5 years), using the equivalent 1 MeV electron fluences estimated for the mission and their corresponding degradation factors;
(ii) 70 °C operating temperature, using the temperature coefficients for the electrical parameters from Ref. [16];
(iii) normal incidence of solar radiation. A further factor associated with actual incidence angles of the solar radiation is considered (see Table 3).

The following factors have also been considered for the simulation:

(a) a random experimental error on $I_{sc}$ and $I_{mpp}$, to consider additional mismatch factors associated with measurement errors during the classification procedure;
(b) a series resistance of 0.37 Ω for the strings and 0.15 Ω for the modules, associated with wires and connectors.

Fig. 2 shows a typical $I$–$V$ curve for a mean module at EOL and 70 °C. It should be mentioned that this curve represents the $I$–$V$ values generated by the module in the bus bar of the satellite, because it includes losses in blocking diodes, wires and connectors.

Three solar arrays were generated using different classification criteria for the solar cells: $I_{mpp}$, $I_{sc}$ and $P_{mpp}$. Table 1 shows the mean power at EOL and 70 °C obtained for each case. The maximum power is obtained using the $I_{mpp}$ classification criterion, even though the difference of the results using different classification criteria is less than 2%.

The influence of the experimental errors during the classification procedure on the expected power generation was also analysed. A random error of 2%, 4% and 6% was introduced in $I_{sc}$ and $I_{mpp}$ for each cell. As experimental errors in voltage measurements are usually much lower than in current measurements they have not been included in the simulations. Table 2 shows an example of the variation of the electrical characteristics of a module at BOL
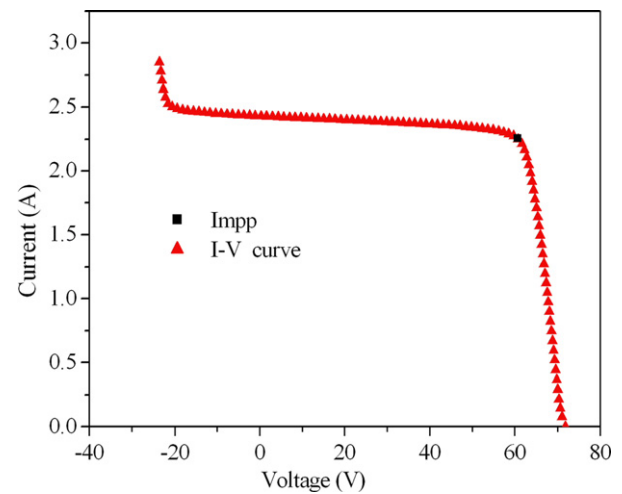


**Fig. 2.** Typical $I$–$V$ curve for a 5 strings module and 32 cells per string, at EOL and 70 °C.

**Table 1**
Electrical characteristics of the mean module obtained using different classification criteria.

| Classification criteria | Power at $P_{mpp}$ [W] |
|---|---|
| $I_{mpp}$ | 3268 |
| $I_{sc}$ | 3241 |
| $P_{mpp}$ | 3232 |

**Table 2**
Influence of the simulated experimental errors on the electrical parameters of one module. Percentage differences are shown in parentheses.

| Error | $V_{oc}$ [V] | $I_{sc}$ [A] | $P_{mpp}$ [W] | $V_{mpp}$ [V] | $I_{mpp}$ [A] |
|---|---|---|---|---|---|
| 0% | 83.42 | 2.379 | 165.0 | 73.62 | 2.241 |
| 2% | 83.43 | 2.396 | 164.0 | 73.73 | 2.224 |
| | (0.01%) | (0.7%) | (−0.6%) | (0.2%) | (−0.8%) |
| 4% | 83.44 | 2.418 | 163.0 | 73.93 | 2.205 |
| | (0.02%) | (1.6%) | (−1.2%) | (0.4%) | (−1.6%) |
| 6% | 83.45 | 2.432 | 160.9 | 74.11 | 2.171 |
| | (0.03%) | (2.2%) | (−2.5%) | (0.7%) | (−3.1%) |

and 28 °C, as a function of the experimental errors considered. These results are similar for other operating conditions and could be summarised as follows:

- $I_{mpp}$ and $P_{mpp}$ decrease less than half the experimental error considered;
- $I_{sc}$ increases less than half the experimental error considered;
- $V_{oc}$ and $V_{mpp}$ are almost independent on the error.

In order to estimate the number of strings needed to satisfy the power requirements of the mission, the $I$–$V$ curve for the mean module has been obtained for the worst case: EOL (5 years) and maximum duration of eclipses (December 21st), which also corresponds to the maximum angle of incidence of the solar radiation.

Taking into account that the $I$–$V$ curve of the module has been obtained for normal incidence of a solar radiation of 1367 W/m$^2$, the factors associated with: (i) non-normal incidence, (ii) the variation of the solar radiation during the year, and (iii) the eclipses, should be added. Moreover, an additional degradation factor associated to damage due to UV and micrometeorites has also been introduced.

Using the factors shown in Table 3 and considering a battery voltage of 61.4 V, the orbital mean power generation for the mean module (5 strings) is about 94 W for the worst case. Taking into
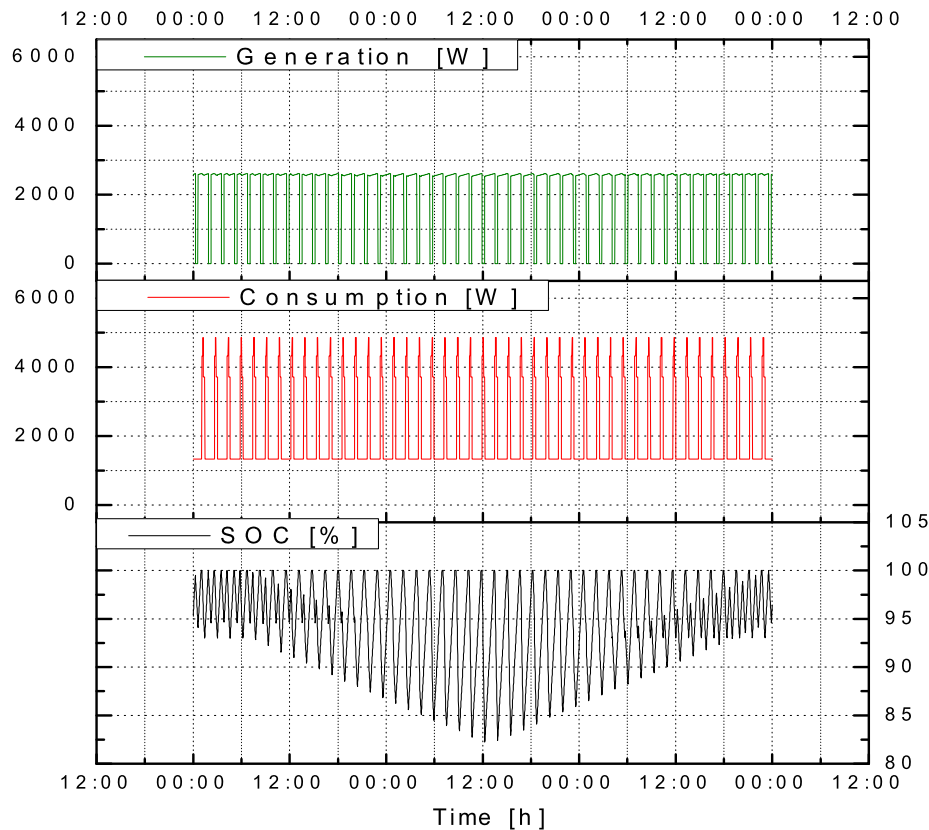
**Fig. 3.** Consumption, array generation and SOC on December 20th to 22nd (worst case) for the SAOCOM 1A.

**Table 3**
Factors for the estimation of the mean module power generation in December at EOL.

| | |
|---|---|
| Distance Sun–Earth | 1.029 |
| Solar radiation incidence angle (31°) | 0.857 |
| Rate of illumination | 0.796 |
| UV + micrometeorites | 0.980 |
| Total | 0.688 |

account a mean power requirement of 1900 W a minimum of 101 strings are needed.

Power subsystem simulations were performed using 112 strings, the maximum number compatible with the available area. As an example Fig. 3 shows power consumption, solar array generation, and the state of charge (SOC) for the worst case (EOL, December 20th to 22nd, as part of a simulation beginning on December 18th and extending over 75 orbits), performing only one antenna operation per orbit. For the consumption profile used, the maximum DOD is under 18% (reached on December 20th), with a mean DOD less than 7%, with the full-power demand satisfied [19].

These results show that the solar array and the battery capacity are appropriate for the consumption considered.

### 2.2. Aquarius/SAC-D mission

SAC-D mission has a similar profile to that of the SAOCOM mission: the orbit is Sun-synchronous, frozen at approximately 657 km height, with an inclination of 98° and an orbital hour of 6 PM for the ascending node. The orbital period is 98 minutes, with variable eclipse periods during 4 months each year at southern latitudes with a maximum duration of 19 minutes on June. For the solar array parallel to the orbit plane (normal mode of operation), the incidence angle of the solar radiation on the solar cells

varies between 31° (June), 15° (December) and a minimum of 4° (March and September). The main instrument of the satellite is the Aquarius (Band-L radiometer), which measures the ocean salinity and Argentine soil humidity. The area of the solar array is about 9 m$^2$, and the battery is also in this case composed of Li-ion cells with a capacity of 65 Ah at EOL.

The main requirements for the Aquarius/SAC-D mission were as follows:

- The Service Platform being capable of providing at least 1320 W of orbital average power at EOL (5 years).
- A solar array able to generate during daylight time a minimum power of 1600 W after 3 years mission, with a Sun pointing angle of 31.4° in the worst-case season, and having lost one module.
- When exposed to the wide energy spectra of electrons and protons in the space environment for a 5 years mission, the solar cells short circuit current, open circuit voltage and peak power should not be degraded more than 1%, 6% and 7%, respectively.

For SAC-D, three different string configurations (with 18, 19 and 20 cells) were analysed at EOL, and two operating temperatures (53 °C – cold case, and 83 °C – hot case). From the point of view of the power generation a configuration with 18 cells per string was recommended. It should be mentioned that during the hot state the operating voltage could marginally shift to the right side of the maximum power point in the *I–V* curve. However, detailed calculations have shown that this configuration fulfil safely the power requirements of the mission [18].

Design and power subsystem estimations were carried out as described in Section 2.1 and led to the following configuration: 2584 cells distributed on 143 strings, each string containing 18 cells interconnected in series. Strings were arranged in

21 modules of 6 strings, 1 of 7 strings and 2 of 20 strings. Table 4 shows the electrical characteristics of the modules simulated using the $I$–$V$ curves measured for each cell at normalised conditions (AM0, 1367 W/m$^2$, 28 °C, and normal incidence of radiation).

## 3. Experimental simulation of in-orbit conditions

### 3.1. Radiation damage

A satellite in a low Earth orbit (LEO) works in a radiation "unfriendly" environment. Inside the inner Van Allen belt there exists isotropic proton and electron irradiation, but most part of the damage is due to protons with energies ranging from a few keV to hundreds of MeV. In addition the satellite is unprotected from cosmic radiation hitting with all kinds of energetic ions.

**Table 4**
Electrical characteristics of the modules simulated using the cell $I$–$V$ curves measured at normalised conditions.

| Module | $V_{oc}$ [V] | $I_{sc}$ [A] | $P$ [A] | $V_{mpp}$ [V] | $I_{mpp}$ [A] |
|---|---|---|---|---|---|
| 1 | 46.9 | 2.90 | 106 | 39.0 | 2.72 |
| 2 | 47.1 | 2.92 | 109 | 39.5 | 2.74 |
| 3 | 46.9 | 2.91 | 107 | 39.0 | 2.74 |
| 4 | 46.9 | 2.91 | 106 | 38.8 | 2.73 |
| 5 | 46.8 | 2.91 | 106 | 38.9 | 2.73 |
| 6 | 46.9 | 3.38 | 125 | 39.2 | 3.19 |
| 7 | 46.9 | 2.90 | 106 | 38.9 | 2.73 |
| 8 | 46.7 | 2.91 | 106 | 39.0 | 2.73 |
| 9 | 46.9 | 2.92 | 108 | 39.5 | 2.74 |
| 10 | 46.8 | 2.91 | 106 | 38.8 | 2.73 |
| 11 | 47.0 | 2.91 | 107 | 39.1 | 2.74 |
| 12 | 47.0 | 2.92 | 109 | 39.6 | 2.74 |
| 13 | 46.6 | 2.87 | 106 | 39.0 | 2.71 |
| 14 | 46.5 | 2.89 | 105 | 38.9 | 2.71 |
| 15 | 46.7 | 2.91 | 106 | 39.0 | 2.73 |
| 16 | 46.4 | 2.91 | 105 | 38.7 | 2.72 |
| 17 | 46.7 | 2.88 | 106 | 39.1 | 2.72 |
| 18 | 46.5 | 2.90 | 106 | 39.1 | 2.72 |
| 19 | 46.8 | 2.41 | 89 | 39.3 | 2.27 |
| 20 | 46.4 | 2.43 | 89 | 39.0 | 2.28 |
| 21 | 46.7 | 2.89 | 107 | 39.1 | 2.73 |
| 22 | 46.7 | 2.90 | 106 | 38.9 | 2.72 |
| 23 | 46.6 | 2.92 | 106 | 39.0 | 2.73 |
| 24 | 46.6 | 2.89 | 107 | 39.2 | 2.72 |

To consider this situation a chamber was built for testing solar cells by cycling the temperature of sample coupons within the expected in-orbit temperature range. At the same time the cells under test are irradiated by a proton beam featuring a space-like spectrum with variable incidence angles to approach the isotropic space flux. Ion beams are delivered to the test chamber by the Tandar 20 MV Tandem Van de Graaff Accelerator. This facility is somewhat similar to that described in Ref. [17], but our upper energy limit for protons is at present 25 MeV, suitable for irradiating samples with 100 to 150 μm thick cover glasses. Attached to the chamber a solar simulator based on a 1 kW Xe lamp (Sciencetech SS 1 kW) allows illuminating the samples with a space-like photon flux.

Fig. 4 shows a picture of the facility. The size of the access lid (on top of the chamber) is 760 mm in diameter, while the ion beam enters through a 5″ diameter port. The ion optics was designed to produce an ion beam of about this size on the target holder. Appropriate shielding collimators were installed to prevent nuclear reaction activation of the stainless steel beam line. The chamber can be lined with aluminium sheet with the same purpose. Some new features have been added, for example the beam line was modified to include a proton energy degrading system. This degrader allows fast modification of the beam energy in order to simulate the space proton spectrum, and also, it allows defocussing the beam to produce irradiation over bigger areas.

In order to improve the dose uniformity a beam sweeping system was developed, consisting in two dipolar magnets (steerers) oriented along the $X$ and $Y$ axes. The magnets are fed by two triangular current waveforms with incongruent periods and used to deflect the beam, which is swept over the target surface. The resulting beam intensity uniformity is better than 5% over the whole target area.

A 9-Faraday cup (FC) array, or Multiple Faraday Cup (MFC), was developed to measure the beam intensity and to determine its uniformity. Data are collected in a personal computer installed in the accelerator control room. Fig. 5 shows the results of a first irradiation test [4]. In this example the two segments reaching values close to 120 pA indicate an unexpected increase of the current and poor uniformity due to beam instabilities. It can be seen that the MFC array is able to give a clear indication of the beam shape and uniformity at the irradiation area.



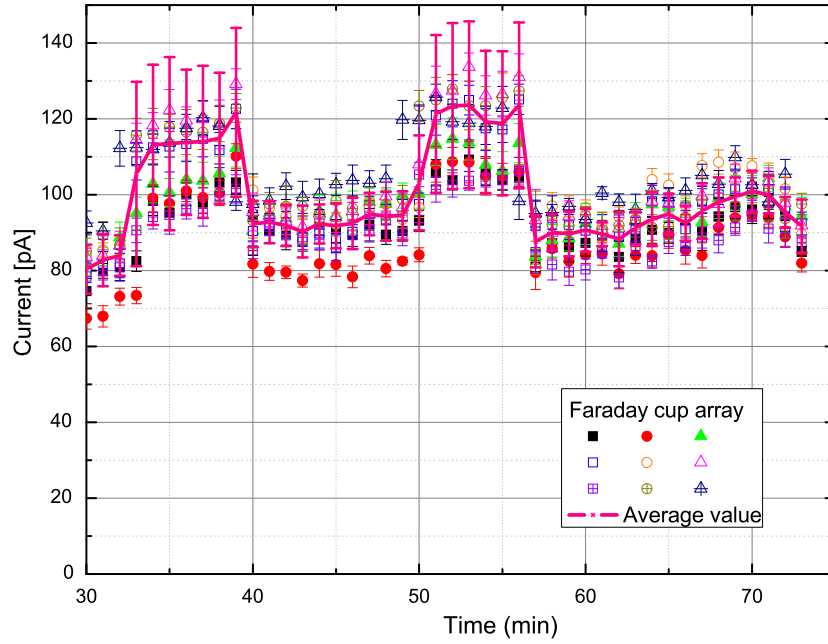**Fig. 4.** 76-cm vacuum chamber installed on one of the Tandar accelerator beam lines.

**Fig. 5.** Sequential measurements of beam currents for the 9 Faraday cups of the MFC array. Each symbol represents the average of twenty individual measurements on each FC, the errors bars correspond to their standard deviation. The solid curve is the average of the current measured by the 9 FCs.
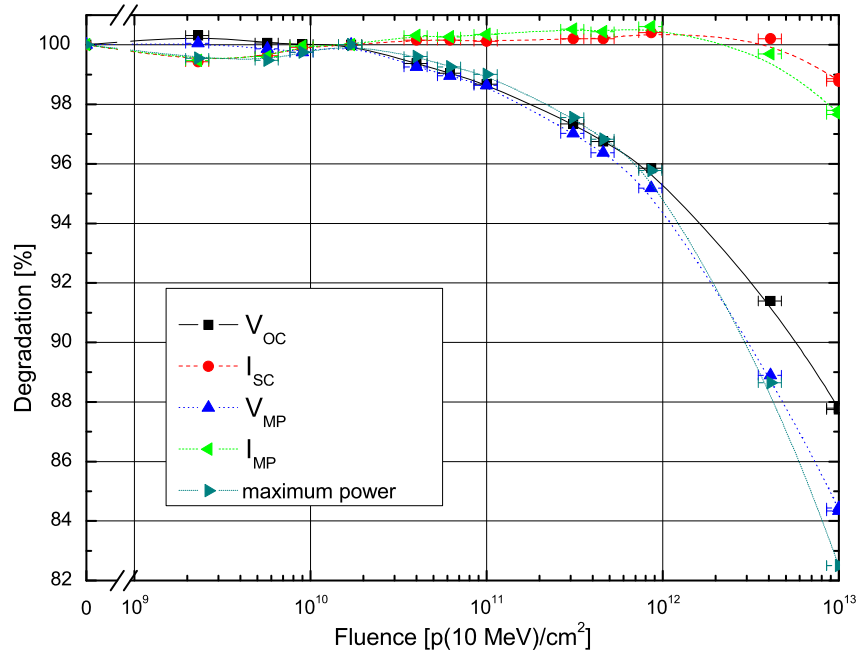


**Fig. 6.** Degradation vs. fluence. The degradation errors are not shown as they are smaller than the symbols.

Equivalent proton fluence and irradiation conditions for mono-crystalline Si solar cells in low Earth orbits have been found using Alurralde's method [1], by comparing the PKA spectra of isotropic incidence low altitude orbit with laboratory monoenergetic proton irradiation. It should be noted that the model is valid only for Si solar cells, as at present it was not yet adjusted to InGaP/GaAs/Ge triple junction solar cells.

The application of the Alurralde's method allows us to draw the following conclusions: (i) fifty percent of the damage is mainly produced by collisions transferring more than 0.7 keV to the cell material in laboratory irradiations. In consequence, cascades play an important role in the production of damage. (ii) The integral

damage efficiency is more than thirty times higher for space irradiation at quasi-polar LEO orbits than for laboratory backside monoenergetic irradiation, see Ref. [1].

For triple junction InGaP/GaAs/Ge solar cells the so-called JPL method was applied [30] as implemented at the Spenvis facility [24], which allows choosing between different types of solar cells. In the present study we selected the cell featuring the most similar characteristics to those of the Emcore ATJ type to estimate the equivalent 1 MeV electron fluence. This result was then converted to its equivalent fluence of 10 MeV protons and this value was used to assess degradation as a function of the fluence measured in the present work. The result is shown in Fig. 6, where each data

point was extracted from the *I*–*V* curve measured using the four-point method and a Model 2602 Keithley SMU, using the solar simulator for illumination. This study was performed "in situ", halting the irradiation at selected fluencies to perform the measurements. The estimated errors in the degradation are smaller than the size of the symbols used in Fig. 6. All irradiations were made using the sample holder with controlled temperature at 30 °C. From Fig. 5 a 15% error in fluence was adopted. Other particular topics on radiation damage studies performed are presented elsewhere [1,3,4,6, 17,31].

### 3.2. Thermal cycling

Due to pass through eclipses, changes of orientation with respect to the Sun, and eventual shadowing, the solar panels in satellites are continuously subjected to thermal cycling between extreme temperatures, which can reach −100 °C and +100 °C. These temperature changes are relatively slow as cooling and heating are essentially due to absorption of thermal radiation from the Sun and, respectively, to radiative emission to space from the panel surface.

Several devices have been built to test solar cells and electronic components under similar thermal conditions to those found in the space environment, but being able to induce much faster temperature excursions.

One of them consists of a sample holder attached to a cold plate with circulating $LN_2$. At the same time a resistive heat source can be activated so that different temperature profiles can be achieved in the holder. By alternating or combining cooling and heating sources, the thermal cycles found in space applications can be simulated by this device, which works either in a controlled atmosphere plastic chamber, where cycling periods of the order of 20 min were performed [5].

A similar method for heating/cooling was used in a sample holder installed in the in-line 76-cm vacuum chamber, where slow vacuum cycling was performed on solar sensors under specified temperature ramps.

In order to run a larger number of thermal cycles a fast thermal shock device was built, using a specially designed $LN_2$ nozzle and 350 °C heat guns under automated control. Fast cycling was achieved by removing the honeycomb and supporting the solar cell strings only by a thin carbon fibre substrate covered with a Kapton film. The reduction in the associated thermal mass allowed very fast cycling (of the order of 2 min) within the same temperature interval.

Using this device, over 3000 thermal vacuum cycles were performed between −100 °C and +100 °C on a substring of 16 ATJ solar cells integrated at CNEA in a dry nitrogen gas atmosphere at 1 atm pressure, and other sample, with 18 flight cells, was successfully qualified by 5000 thermal cycles between −50 °C and +80 °C. These tests allowed validating the developed bonding techniques, interconnector integrity, welding, soldering, and bonding processes, both for cells and coverglasses. The number of cycles performed was comparable with the number expected in the whole mission lifetime. All these fast cycling tests have been performed in dry nitrogen gas atmosphere, at a pressure slightly higher than 1 atm.

The solar cells are mounted according to developed integration procedures (see Fig. 7). This picture has been obtained during visual inspection after the first 2000 thermal shocks. Observe the bypass diodes welded on the cell corners, and the 4 surface mounted $Pt_{100}$ temperature sensors. Temperature measured by $Pt_{100}$ sensors and bidirectional electric continuity using a square wave current of about 0.45 A peak are permanently monitored and recorded using an 8-channel data logger with 1 s sample time. This checks the integrity of the bypass diode connections. The control of electrical
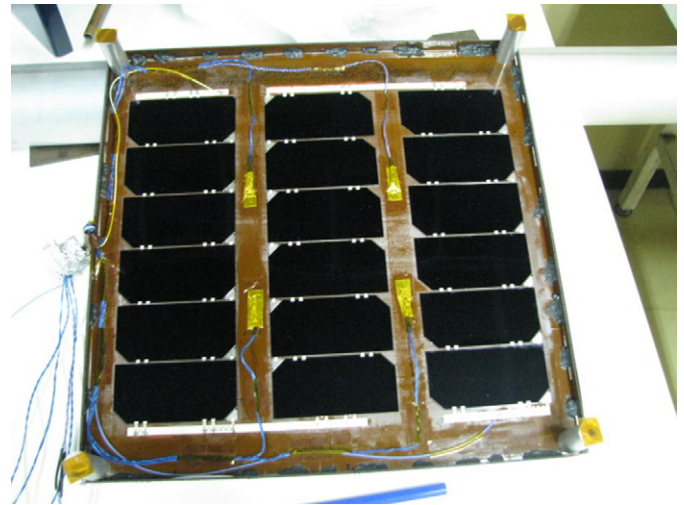


**Fig. 7.** Coupon containing 18 series-connected Emcore ATJ cells on a carbon fibre skin of the honeycomb.

**Table 5**
Summary of the result of a thermal cycling test performed on a 4-cell coupon.

| Component | Before test | After test |
|---|---|---|
| Interconnectors | OK | OK |
| Current collectors | OK | OK |
| SCAs | OK | 2 cracked glass |
| $Pt_{100}$, cables | OK | OK |
| Soldering | OK | OK |
| Substrate | OK | OK |

continuity has shown no noticeable degradation in the different tests performed, and visual inspections at regular intervals during the long tests have shown only minimal chippings on coverglasses. Preliminary results were presented in [4], and a sample of thermal cycling results is summarised in Table 5.

## 4. Processes for solar array integration

### 4.1. Interconnectors

For the interconnection of cells metallic tabs are commonly used. Silver-plated molybdenum and Kovar were selected as the base material. Mo and kovar are used due to their high resistance to fatigue. Moreover, the first material is non-magnetic. Interconnector fabrication from Mo and Kovar sheets is performed in three stages: sheet electroplating, cutting, and forming. Two electroplating processes were developed for both materials. Results are evaluated by optical and SEM observations. Besides, a testing machine was developed in order to assess the fatigue resistance of interconnectors, this machine produces an alternating displacement of ±50 μm, emulating the effect of the thermal cycling suffered in orbit. Test results show that interconnectors made using with this procedure withstand more than 100,000 cycles.

Devices for cutting and conforming appropriate interconnectors for the chosen solar cells were developed and constructed. Thermal cycling tests made on coupons assembled with Kovar-plated interconnectors showed good behaviour after more than 10,000 cycles. This type of interconnectors was used for (i) the integration of one of the two strings of the second engineering model made to undergo the set of tests described below, (ii) for the Engineering Qualification Model (EQM), and (iii) for the SAC-D mission [4] Flight Model (FM).
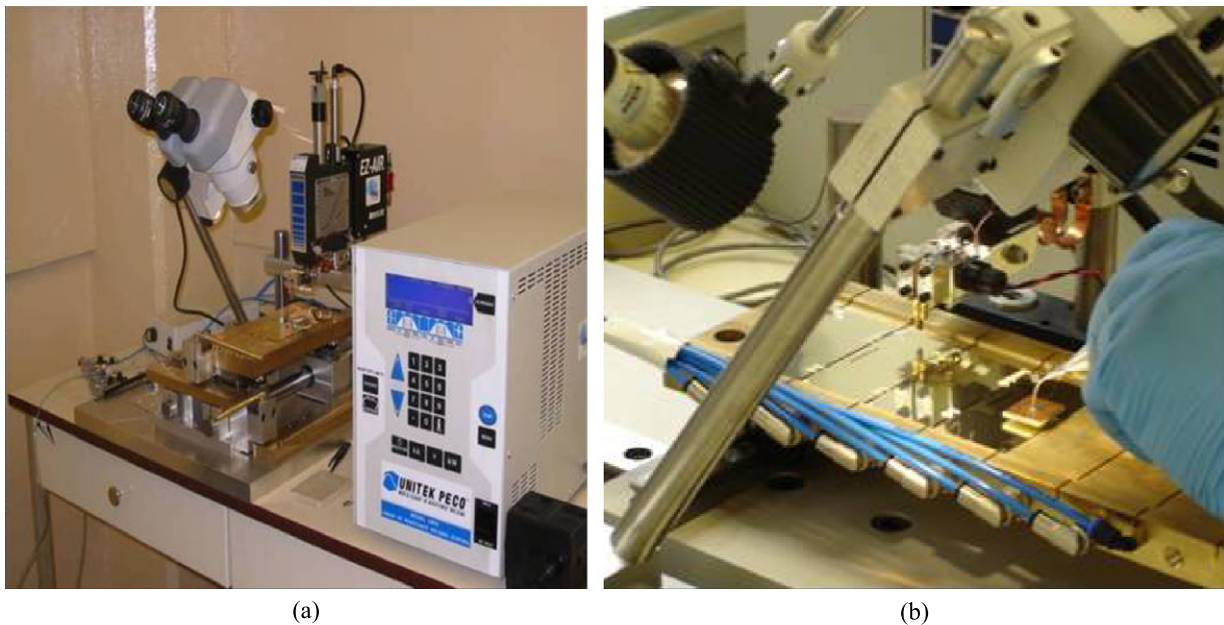
(a)                                    (b)

**Fig. 8.** (a) Welding system. (b) Soldering process.

### 4.2. Welding and soldering joints

#### 4.2.1. Front side welding

The welding for solar cells interconnection must guarantee an adequate electrical contact and enough strength to resist the stresses commonly produced at the launch and during in-orbit operation.

The resistance, parallel-gap welding technique was selected for welding the silver-plated Kovar interconnectors to the front side of ATJ Emcore solar cells [11–13,20,27,29]. The system used for welding consisted of a programmable DC power supply (Model DC 25) and a parallel-gap welding head (Model 86A/EZ) made by Unitek Co. (Fig. 8a). It allows programming the welding cycles, number of pulses, pulse amplitude, pulse time, modes of current flow, weld force, magnitude/time, etc. Optimum process parameters were identified in order to both, assuring stable welding conditions, and producing joints of high integrity. Previously to welding the surface condition of contacts was checked.

Pull tests at 45° angle were performed for assessing welding quality and strength. All tests were carried out using a small motor driven machine specifically designed and constructed with this purpose. In the case of the 45° tests all pulling strength results satisfied a requirement of 350 g established in this laboratory.

To allow comparison with data supplied by Emcore, welding pull tests were conducted at 0° pull angle. Tests at 0° performed on about 250 cells in the frame of the SAC-D FM integration showed a Gaussian-like distribution centred at 985 g [4]. Results are shown in Fig. 9.

The standard deviation $\sigma$ was about 240 g, therefore 68% of the tested samples gave results between 745 and 1225 g. The minimum value registered was approximately 400 g, higher than the acceptable minimum. For the welding of joint-interconnecting Si-bypass diodes, the mean value obtained for traction tests was 700 g.

#### 4.2.2. Back side soldering

Soldering is a reliable, established process, which has been successfully used well for past arrays [29]. For this work, it was ver-
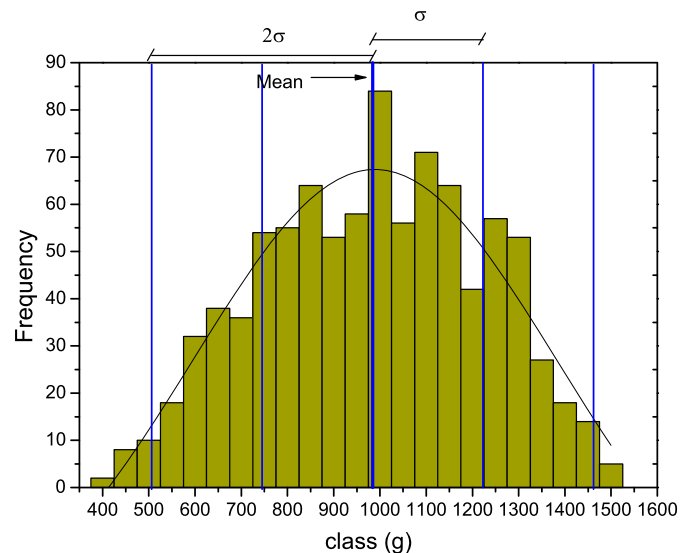


**Fig. 9.** Distribution of results of pull tests.

ified that the welding made to the smoother cell contact surfaces were very much stronger than those made to the rougher back side cell surface. Moreover, measurements showed that the roughness of the back side of the cell is almost five times greater than that of the front side. It was proved that higher electrode pressures somewhat improve welding strength; however, the presence of the coverglass adhesive hinders the increase of that pressure. Because of this, soldering was chosen for the interconnections on the back side (Fig. 8b).

The joints were made with a programmable reflow Unitek system with controlled temperature profile and solder preforms consisting of a Sn/Pb/Ag alloy. The principal parameters of the system were thermode type and force, temperature and time.

The quality of welding and soldering processes was assured by verifying the actual power or temperature profiles during the processes, and through periodic pulling tests and visual inspection of imprints.

*4.3. Bonding*

Solar cells in space applications are protected by coverglasses from UV exposure and from low energy charged particles. A 100-μm coverglass is mounted onto each cell.

Activities related to bonding techniques can be listed as:

- bonding coverglasses to cells,
- bonding stringed cells to substrate,
- bonding buses to substrate,
- bonding cables and electronic devices to substrate.

Methods, devices and procedures must be highly reliable. To bond coverglasses, a special system was developed, consisting of: an adhesive distributor pneumatically controlled (Fig. 10), a motorised electronic controlled device for horizontal motion, and a device for positioning and aligning the coverglass on the cells. Two methods were developed for this operation, one to bond coverglasses in air and the other in a vacuum chamber (Fig. 11).
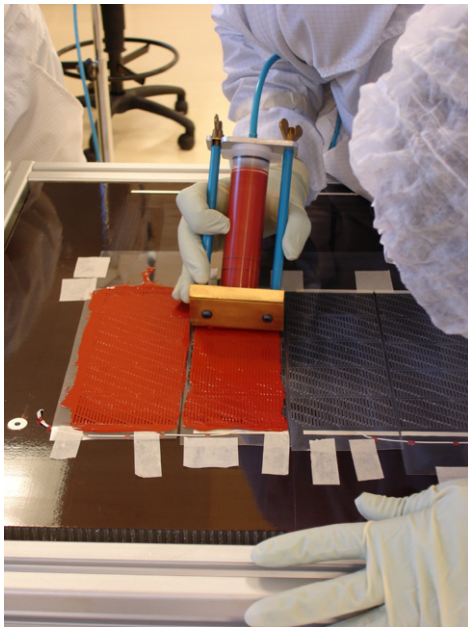


**Fig. 10.** Adhesive distributor.
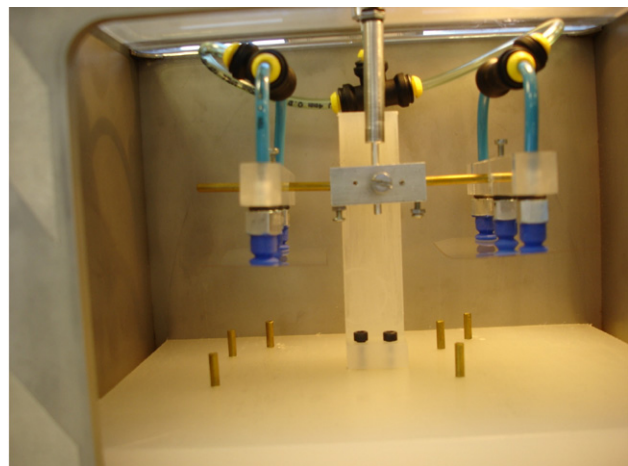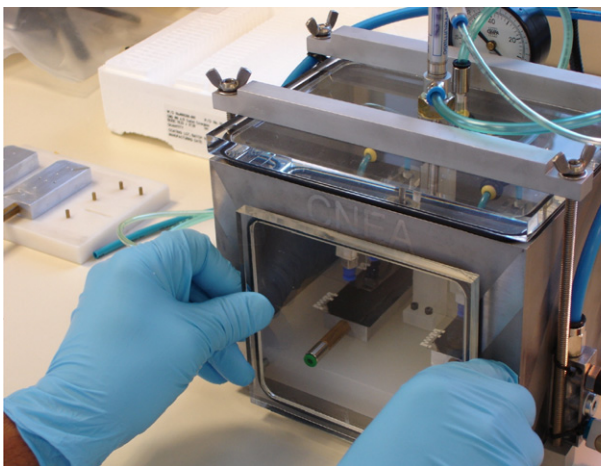
Substrings of cells are bonded to the substrate using specially designed masks and adhesive dispensers. In all cases space-qualified adhesives were used.

## 5. Engineering models integration and characterisation

Space SCA integration could be resumed by the following steps:

- SCA formation (cell + welded frontal interconnectors + bonded coverglass),
- $I$–$V$ measurement and classification,
- stringing of SCA's,
- cables and strings, bonding to substrate.

In order to make a preliminary qualification of the procedures developed, two engineering models, EM#1 and EM#2 were designed, constructed, and characterised.
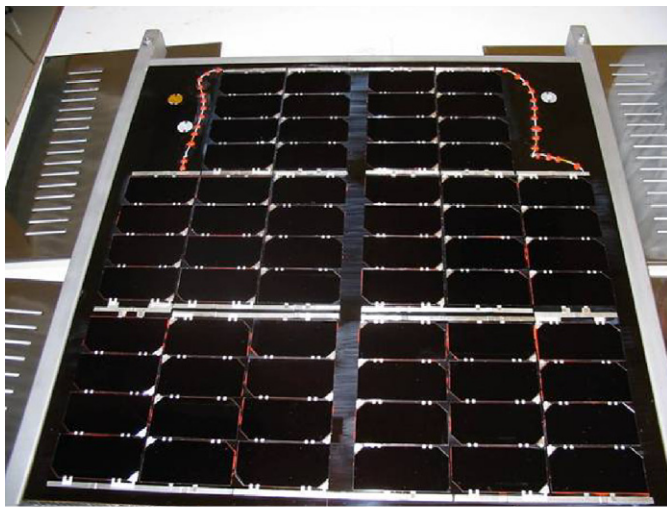
EM#1, shown in Fig. 12a, has two strings, each one composed of 32 series-connected Emcore ATJ solar cells. The cells were arranged in 8 substrings of four cells. The module, of 520 mm × 520 mm, was built on an aluminium honeycomb substrate, with carbon fibre skins and a self-adhesive Kapton sheet for electrical insulation.

Each SCA was electrically measured using a TS-Space Close Match solar simulator at $T = 28\,^\circ$C and with 1.367 kW/m$^2$ (equivalent to AM0 irradiation). According to the data obtained the SCA's were classified on the maximum power basis. Substrings of four cells each were soldered and interconnected through a bus architecture, resulting finally in two strings of 32 cells each. This arrangement matches the requirement of the solar array design for the SAOCOM mission.
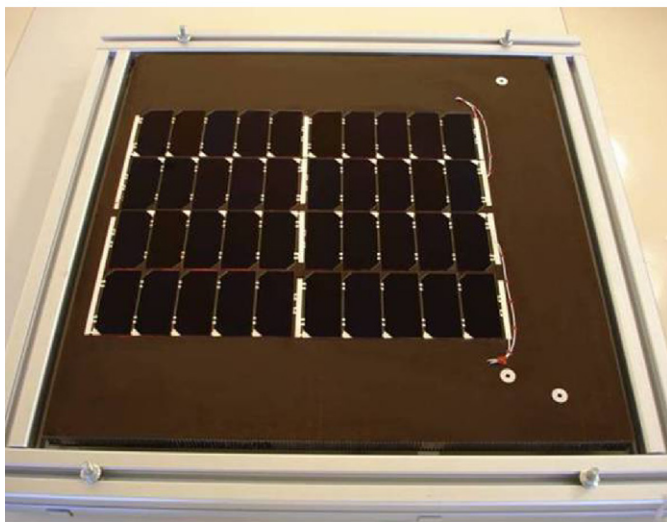
Once the substrings were assembled, all of them were verified by measuring their $I$–$V$ curves using the solar simulator. The proper function of bypass diodes was also verified by measuring the $I$–$V$ curve of all substrings darkening successively each cell. An example of the results obtained is presented in Fig. 13.

The second engineering model (EM#2) was assembled within a similar concept, but strings were built of 20 cells with substrings of five cells each in order to match preliminary requirements of SAC-D mission. As mentioned in Section 4.1, one of these strings was integrated using interconnectors fabricated at CNEA.

Electrical characterisation of both engineering models was achieved by the measurement of the $I$–$V$ curves using a pulsed light source (a commercial photographic flash), a neutral filter, a digital oscilloscope, and an electronic load. Measurements were made at ambient temperature ($T = 22.5\,^\circ$C $\pm\ 1\,^\circ$C). The



**Fig. 11.** Vacuum chamber for coverglass bonding.

(a)



(b)

**Fig. 12.** Engineering models finished: (a) EM#1, (b) EM#2.



**Fig. 13.** *I–V* measurement of one substring of EM#1, including the verification of the bypass diodes performance.
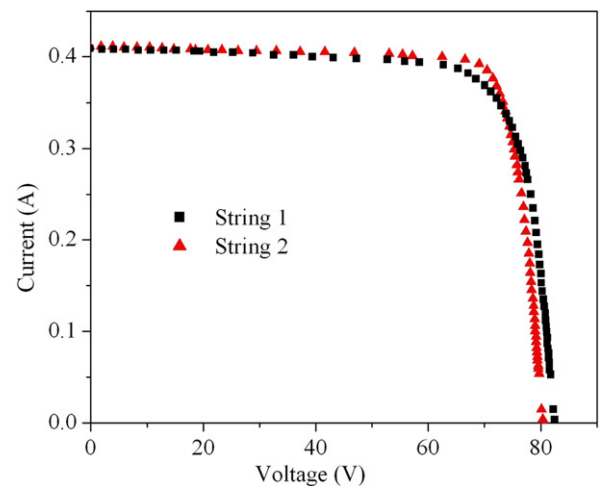


**Fig. 14.** *I–V* measurement under sunlight for EM#1.

*I–V* curve for the EM#1 was also measured under sunlight at $(888 \pm 18)$ W/m$^2$ of irradiance and AM1.62 spectrum, resulting $V_{oc} = 82.5$ V and $I_{sc} = 0.408$ A for string 1, and $V_{oc} = 80.4$ V and $I_{sc} = 0.411$ A for string 2. The results of these characterisations are shown in Fig. 14.

Vibration and thermal vacuum tests were performed at the INVAP S.E. facilities, San Carlos de Bariloche, Argentina. Natural frequencies were determined, being the models subjected to sinusoidal vibrations along the *Z* axis with accelerations of 25-, 50-, 74- and 100-times *g*. A random scan beyond the natural frequencies was also performed, representing the vibration spectrum of the vector Cyclone-4 at launching condition.

Previous to tests, EM#2 had been observed to have the following defects: bubbles in the adhesive for some cells, some amount of solid debris between the cell and glass, and one chipped cell. However, in all cases the module met the acceptance criteria. After tests, the model did not show new defects.

Later, 10 thermal cycles between $-100\,°C$ and $100\,°C$ were made at an average pressure of $1 \times 10^{-5}$ Torr, and the results of both tests were evaluated by visual inspection (using a $10\times$ magnifier) and by pulsed light electrical characterisation. As can be seen in Figs. 15 and 16, the results before and after the tests did not reveal relevant differences. Thus, these results have been considered as a preliminary qualification of the components and
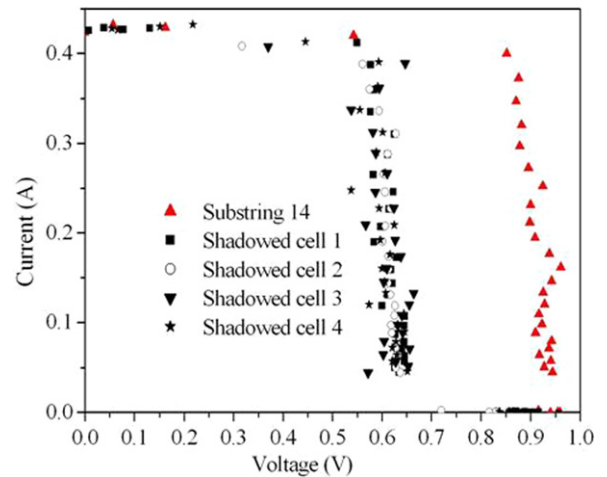
procedures, and the fabrication procedures were accepted as applied on both engineering models.

Further-on, a third engineering model, EM#3 (see Fig. 17) was assembled, characterised, and tested. This model is composed of 6 strings arranged from 3 substrings of 6 series-connected ATJ cells each (total: 108 cells). Two pairs of coarse solar sensors (CSS) were mounted at the corners of the substrate. Also in this case the substrate is an aluminium honeycomb with carbon fibre skins and a Kapton sheet on the front side.

Electrical verification was performed according to internal procedures using a pulsed flash lamp illumination. The corresponding *I–V* curve for the EM#3, obtained by this method, is shown in Fig. 18.

Qualification tests on EM#3 were performed in the *Laboratório de Integração e Testes* (LIT) of the *Instituto Nacional de Pesquisas Espaciais* (INPE), São Paulo, Brazil. These tests included static and dynamic vibration, acoustic tests, and thermal cycling in vacuum, in order to qualify the model fabrication procedures as well as the components utilised.

Visual inspection of the solar cells and CSSs mounted in EM#3, as well as all components (resistors, diodes, connectors) showed that no relevant changes were produced after environmental tests respect to the initial state. Table 6 describes the initial status before tests and the acceptance criteria for each component. These results allow concluding that the EM#3 model qualifies from visual inspection acceptance requirements.
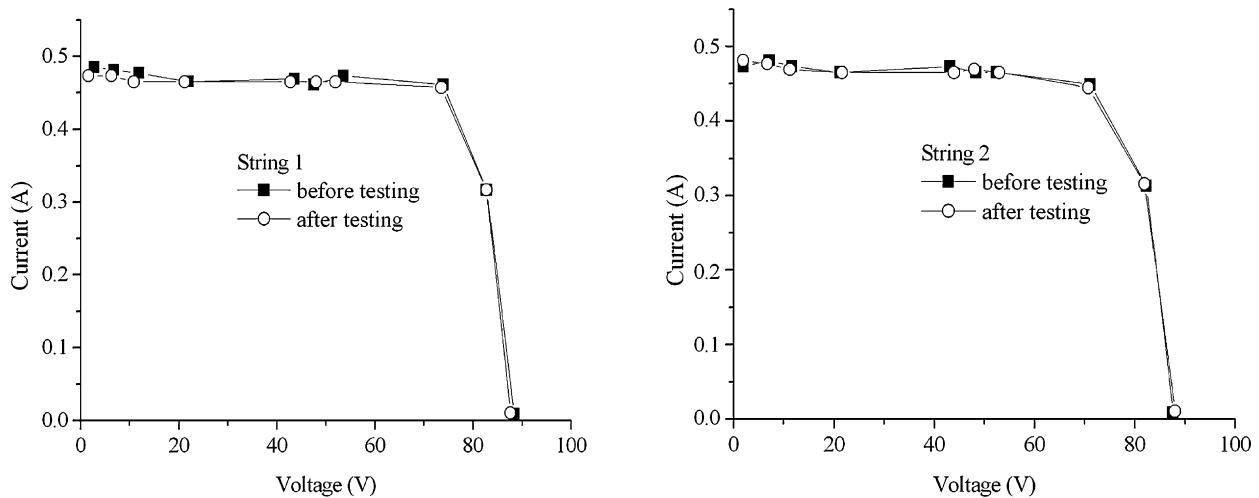
**Fig. 15.** $I$–$V$ characteristic of strings 1 and 2 from EM#1 before (filled symbols) and after (open symbols) thermal and vibration tests.
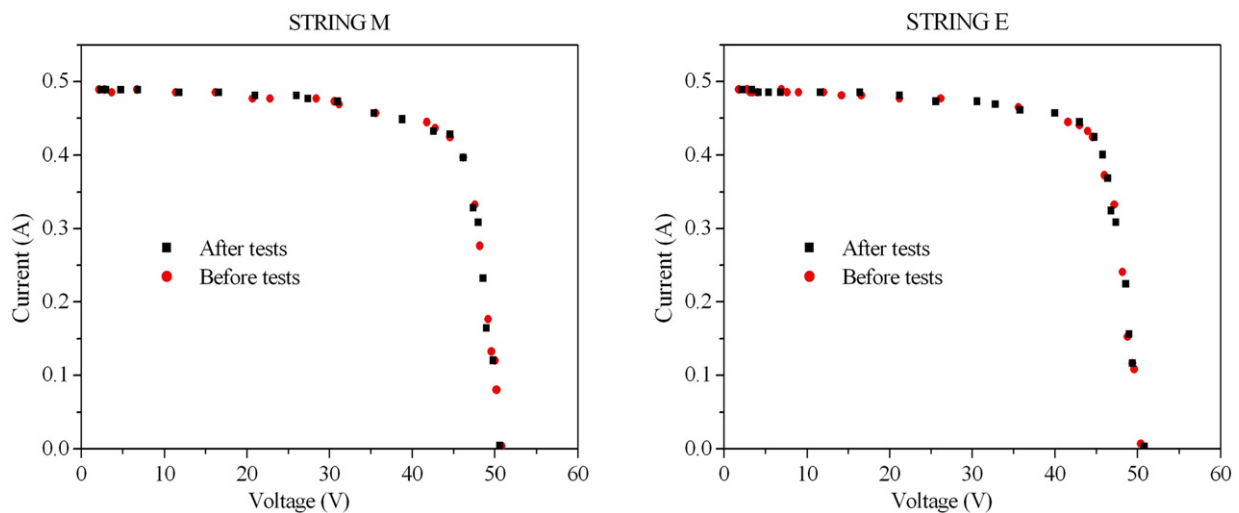


**Fig. 16.** $I$–$V$ characteristic of string M (integrated with CNEA interconnectors) and E (integrated with Emcore interconnectors) from EM#2 before (circles) and after (squares) thermal and vibration tests.
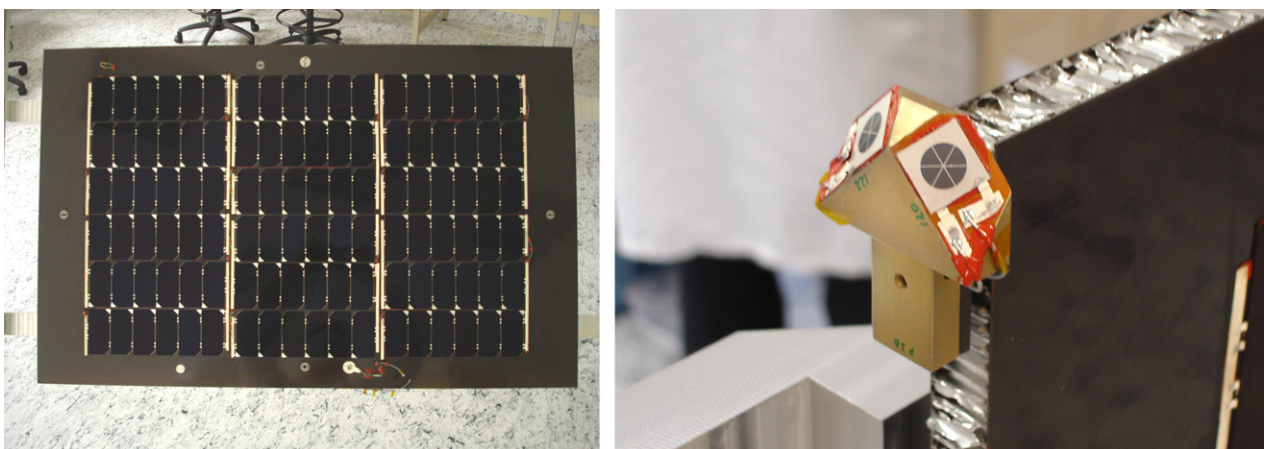


**Fig. 17.** Engineering model #3 (left), and coarse solar sensors mounted on this model (right).

From the electrical point of view, the EM#3 model did not present anomalies when $I$–$V$ measurements after and before the tests were compared. The corresponding $I$–$V$ curves are presented in Fig. 19, where several measurements made before and after tests were superposed. These results show that also from the electrical point of view the model passed the qualification test.

Also a long term thermal cycling test in vacuum (1195 cycles) was performed on EM#3, and again, no relevant differences were found in the visual inspection and electrical verification performed before and after the test.

Although no particular humidity tests have been performed, it should be remarked that all components used for models

**Table 6**
Status previous to tests and acceptance level for each component corresponding to the EM#3 model.

| Component | Before tests | Acceptance level |
| --- | --- | --- |
| Interconnectors | OK | Defective interconnectors: No more than 2% of total |
| Current collectors | OK | Defects not allowed: <br> • Soldering paste or adhesive blocking the release loop <br> • Cracks, fractures, or breaks <br> • Foreign materials on the soldering region or release loop |
| SCAs | Cracked/chipped glass: 0.9% (1 cell) <br> Bypass diodes cracked: 0% <br> Bubbles or cluster of bubbles: 9.2% of total, <br> 1 bubble per cell in average <br> OK <br> Cracked/chipped cells: 0% | No more than 3 per glass <br> Not allowed <br> Maximum projected area should not exceed 0.2% of total cell area <br><br><br> Any class of crack should not exceed 2 per cell |
| CSS | OK | Idem SCA |
| Blocking diodes, resistors, cables | OK | Any cable should not have the following defects: <br> • Curves, torsions, loops or bends excessively sharp <br> • Adhesive delaminating or poor adhesive adherence <br> • Attrition, abrasion, cracks or breaks on the sheath cables |
| Soldering | OK | • It should not present a soldering paste excess beyond the interconnector <br> • Interconnectors should not have deformations that could potentially affect the string integrity or the string adhesion on the substrate <br> • Cracks generated from the soldering points are not allowed |
| Substrate | OK | The insulator (Kapton) should not present evidence of delamination |
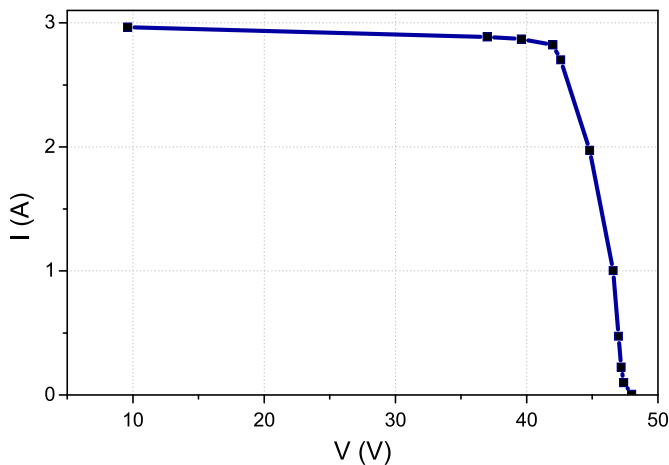


**Fig. 18.** Current–voltage curve ($I$–$V$) measured for the engineering model #3.
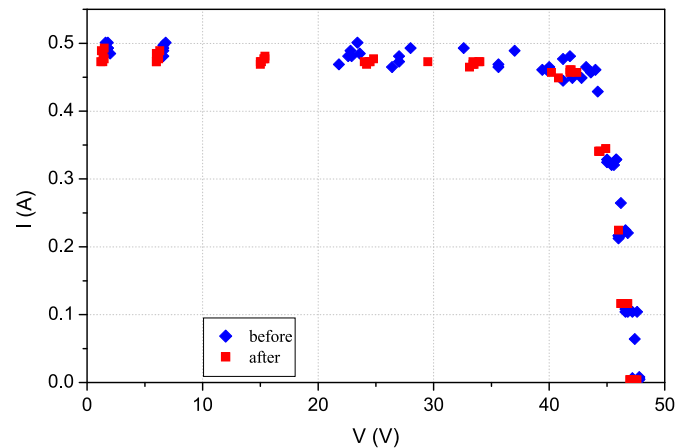


**Fig. 19.** Current–voltage curve ($I$–$V$) of EM#3 after and before tests.

**Table 7**
Summary of construction details of SAC-D FM.

| | |
| --- | --- |
| Solar cells | advanced triple junction (ATJ) solar cells with Si bypass diodes, supplied by Emcore |
| Interconnectors, busses | silver-plated Kovar |
| Si coarse Sun sensors (CSS) | developed and manufactured at CNEA |
| Welding technique | 2 steps pulsed process used for joining the interconnectors to the front side of the cells, validated by visual inspection, electrical characterisation of welded cells, and pulling tests at 0° |
| Coverglass bonding | performed in vacuum, validated by visual inspection and tensile stress |
| SCA | visually inspected, electrically characterised |
| Substrings | integrated after classification using a soldering technique |
| Connectors | soldering the substring terminal interconnectors to the buses |
| Electrical functional tests | performed on all FM modules using Xe-pulsed light |
| FM acceptance tests component & system levels | performed at LIT Laboratory (INPE), Brazil |

integration were space-qualified, and some of them, like coverglasses and solar cells, had been certified by the provider as subjected to humidity tests.

Finally, the Engineering Qualification Model (EQM) associated to the SAC-D mission was constructed and tested. It had the same mechanical characteristics of one wing of the SAC-D solar panel and was partially populated with ATJ solar cells, with a configuration of 18 cells per string. This model successfully passed the

environmental (vibroacoustic and thermal vacuum) tests. These results have been presented elsewhere [2]. Provided that these stages completed satisfactorily the qualification process the next step was the integration of the Flight Model (FM) for the SAC-D mission.

The characteristics of the SAC-D FM are shown in Table 7, where a brief summary of the previously described technology employed in the integration of the SAC-D FM is presented. A more detailed description can be found in [4].
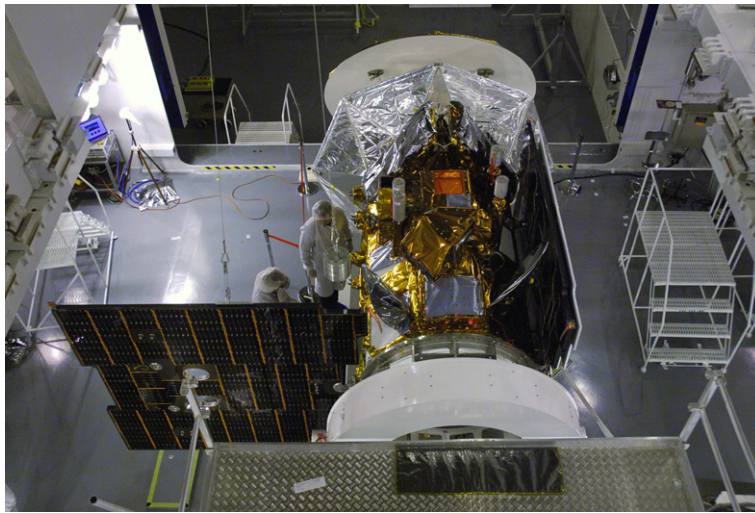
**Fig. 20.** Solar panels mounted on SAC-D satellite, at the launch site at Vandenberg, California, USA.[2]

A double floor container for solar array transportation was designed and constructed, being able to keep environmental condition under specifications during transport and temporary storage. This was indicated in different sensors and registers built in the container.

All satellite components were transferred to the Vandenberg Air Force Base, California, USA, where the SAC-D satellite has been successfully launched on June 10th, 2011, by a Delta II rocket.

Fig. 20 shows the solar panels mounted on the SAC-D satellite at the launch site.

In order to verify the correct performance of each module before switching-on the instruments, telemetry data for different periods were analysed. In what follows the data from September 12 (15 orbits) are considered. In Fig. 21, the current intensity values and the operating temperature obtained by telemetry for the 15 orbits are given for modules 6 (7 strings in parallel), 11 (6 strings in parallel), and 24 (6 strings in parallel), as a function of the angular position of the satellite measured with respect to the North Pole. Negative angles represent the ascending node (travel from South to North at the exit of eclipse), while the descending node is represented by positive angles (going from North to South). The dispersion observed in the values of temperature and current intensity shows the variations of these parameters during this period. For reference, the graphs indicate the short circuit current ($I_{sc}$) and the current at the maximum power point ($I_{mpp}$) obtained by simulation for the modules. The Earth albedo had not been taken into account because of its variability [15] but the Sun–Earth distance correction factor, the radiation incidence angle, and the operation temperature were considered. Fig. 21 shows that:

- The current intensity varies along the orbit due to the albedo. It is observed that the contribution of the albedo is added on top of the 'base' current generated by direct solar radiation.
- The 'base' current of module 6 corresponds to an operating point between $I_{mpp}$ and $I_{sc}$, which means that it constantly provides the generated power.
- The 'base' current of module 24 corresponds to short-circuited condition (not all the available solar array power was required).

- The 'base' current of module 11 oscillates between an operating point and $I_{sc}$, indicating that the module is the commutable unit handled by the regulator.
- The temperature observed near the short-circuited module is higher than the temperature in the proximity of modules in other operating conditions. This is compatible with the fact that the first one dissipates all the power in the solar panel.

Telemetry data analysis for the first stages of the mission shows the correct performance of all modules.

## 6. Conclusions

Qualification of processes and components for space solar arrays was accomplished using several coupons, three engineering models and a qualification model integrated using processes specially developed with this purpose. Visual inspections and electrical verifications before and after vibration and thermal cycling tests did not reveal relevant differences in any case.

Computational codes for design and performance simulation of solar arrays were developed, and radiation damage studies and thermal cycling facilities were set up for testing solar cells and/or electronic components.

Finally the Flight Model for the SAC-D mission was integrated and tested and, on June 10th, 2011, the SAC-D satellite has been successfully launched. Preliminary analysis of telemetry data has shown a proper performance of the solar modules, in good agreement with previous theoretical estimations. As a conclusion it can be stated that the SAC-D solar array is fully operational after the satellite launching.

---

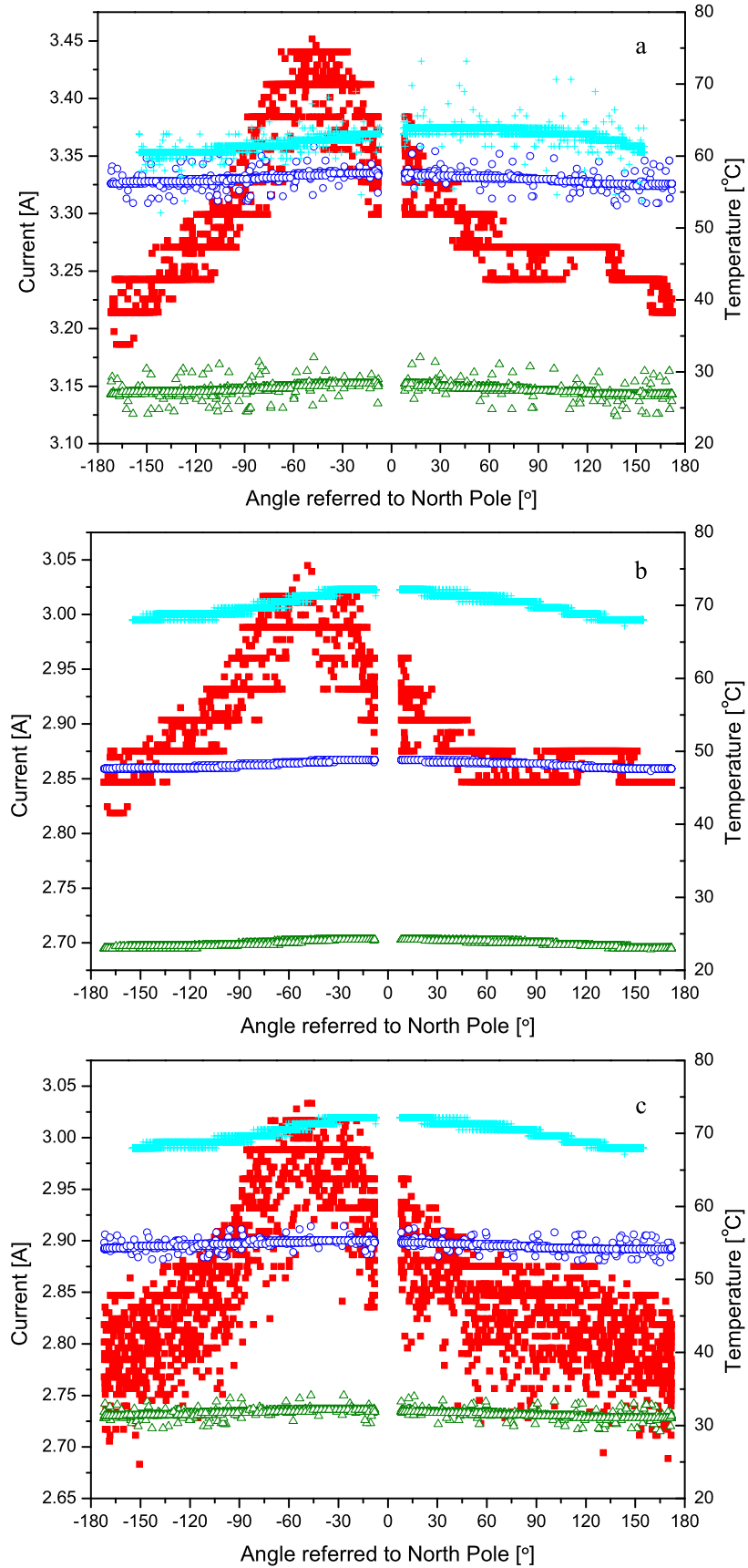[2] http://www.nasa.gov/images/content/542441main_2011-04-28-1_full.jpg.

**Fig. 21.** Current (red squares) generated by modules 6 (a), 24 (b), and 11 (c), and temperature (cyan crosses) on orbits for 12 September 2011. For reference, simulated $I_{sc}$ (blue circles) and $I_{mpp}$ (green triangles) are indicated. (For interpretation of the references to color in this figure legend, the reader is referred to the web version of this article.)

# References

[1] M. Alurralde, Method using the primary knock-on atom spectrum to characterize electrical degradation of monocrystalline silicon solar cells by space protons, Journal of Applied Physics 95 (2004) 3391.

[2] M. Alurralde, M. Barrera, C.G. Bolzi, C.J. Bruno, P. Cabot, E. Carella, J. Di Santo, J.C. Durán, J. Fernández Vázquez, A. Filevich, C.D. Franciulli, E.M. Godfrin, V. Goldbeck, L. González, A. Iglesias, M.G. Martínez Bogado, E. Mezzabolta, A. Moglioni, S. Muñoz, C. Nigri, S.L. Nigro, J. Plá, I. Prario, M.C. Raffo Calderón, D. Raggio, C. Rinaldi, S.E. Rodríguez, H. Socolovsky, M.J.L. Tamasi, Solar array qualification models for Aquarius/SAC-D satellite mission, in: Proceedings of the 23rd European Photovoltaic Solar Energy Conference, Valencia, Spain, 2008, p. 785.

[3] M. Alurralde, M. Barrera, C.G. Bolzi, C.J. Bruno, P. Cabot, E. Carella, J. Di Santo, J.C. Durán, J. Fernández Vázquez, A. Filevich, C.D. Franciulli, E.M. Godfrin, V. Goldbeck, A. Iglesias, M.G. Martínez Bogado, E. Mezzabolta, A. Moglioni, C. Nigri, S.L. Nigro, F. Palumbo, J. Plá, I. Prario, M.C. Raffo Calderón, S.E. Rodríguez, H. Socolovsky, M.J.L. Tamasi, A. Vertanessian, Advances in the development of photovoltaics for space applications in Argentina, in: Proceedings of the 22nd European Photovoltaic Solar Energy Conference, Milan, Italy, 2007, p. 687.

[4] M. Alurralde, M. Barrera, C.G. Bolzi, C.J. Bruno, P. Cabot, E. Carella, J. Di Santo, J.C. Durán, J. Fernández Vázquez, A. Filevich, E.M. Godfrin, V. Goldbeck, L. González, A. Iglesias, M.G. Martínez Bogado, E. Mezzabolta, A. Moglioni, S. Muñoz, C. Nigri, S.L. Nigro, J. Plá, I. Prario, M.C. Raffo Calderón, D. Raggio, C. Rinaldi, S.E. Rodríguez, H. Socolovsky, M.J.L. Tamasi, A. Vertanessian, Flight models for the Aquarius/SAC-D satellite mission, in: Proceedings of the 24th European Photovoltaic Solar Energy Conference, Hamburg, Germany, 2009, p. 695.

[5] M. Alurralde, M. Barrera, C.G. Bolzi, C.J. Bruno, J.C. Durán, J. Fernández Vázquez, A. Filevich, E.M. Godfrin, V. Goldbeck, A. Iglesias, M.G. Martínez Bogado, E. Mezzabolta, S.L. Nigro, J. Plá, I. Prario, M.C. Raffo Calderón, S.E. Rodríguez, M.J.L. Tamasi, A. Vertanessian, F. Antonuccio, P. Cabot, E. Carella, J. Di Santo, C.D. Franciulli, A. Moglioni, G. Berbeglia, D. Fernández Slezack, Development of photovoltaic modules for space applications in Argentina, in: Proceedings of the 20th European Photovoltaic Solar Energy Conference, Barcelona, Spain, 2005, p. 538.

[6] M. Alurralde, M.J.L. Tamasi, C.J. Bruno, M.G. Martínez Bogado, J. Plá, J. Fernández Vázquez, J. Durán, J. Schuff, A.A. Burlon, P. Stoliar, A.J. Kreiner, Experimental and theoretical radiation damage studies on crystalline silicon solar cells, Solar Energy Materials and Solar Cells 82 (2004) 531.

[7] M. Barrera, J. García, H. Socolovsky, F. Rubinelli, E. Godfrin, J. Plá, Activities on simulation and characterization of multi-junction solar cells for space applications in Argentina, in: Proceedings of the 23rd European Photovoltaic Solar Energy Conference, Valencia, Spain, 2008, p. 781.

[8] E.V. den Berg, M. Kronn, Algorithms and performance of a space dedicated solar array modeling tool, in: 6th Space Power Conference, 2002, p. 527.

[9] C.G. Bolzi, C.J. Bruno, J.C. Durán, E.M. Godfrin, M.G. Martínez Bogado, L.M. Merino, J.C. Plá, M.J.L. Tamasi, M. Barrera, First experiment of Argentine solar cells in space: modules fabrication, characterisation, and telemetry data analysis from SAC-A satellite, Solar Energy Materials and Solar Cells 73 (2002) 269.

[10] A. Capel, P. Chapoulie, S. Zimmerman, E. Snachís, Dynamic performance simulation of a spacecraft power system, in: 6th European Space Power Conference, 2002, p. 327.

[11] L.G. Chidester, D.R. Lott, Advances in solar cell welding technology, in: 16th Photovoltaic Specialists Conference, San Diego, USA, 1982, pp. 51–56.

[12] C.L. Chu, Weldability of GaAs solar cells on either GaAs or Ge substrates, in: 28th Photovoltaic Specialists Conference, Las Vegas, USA, 1988, pp. 968–973.

[13] C.L. Chu, P. Iles, Control parallel gap welding for solar cells, in: 38th Electronics Components Conference, Los Angeles, USA, 1988, pp. 40–44.

[14] G. Colombo, U. Grasselli, A. De Luca, A. Spizzichino, S. Falzini, Satellite power system simulation, Acta Astronautica 40 (1) (1997) 41.

[15] Earth's thermal environment, extracted from Thermal Environments, JPL D-8160, http://www.tak2000.com/data/planets/earth.htm.

[16] Emcore photovoltaics, http://www.emcore.com/product/photovoltaic.php.

[17] A. Filevich, C.J. Bruno, J. Fernández Vázquez, M. Alurralde, I. Prario, M.J.L. Tamasi, J.C. Plá, J. Durán, J. Schuff, A. Burlon, P. Stoliar, D. Minsky, A.J. Kreiner, R. Mayer, A compact portable set up for in situ solar cells degradation studies, IEEE Transactions on Nuclear Science 50 (2003) 2380.

[18] E.M. Godfrin, J.C. Durán, D. Fernández Slezak, G. Berbeglia, Design and simulation of the power subsystems for two Argentine satellites, in: Proceedings of the 22nd European Photovoltaic Solar Energy Conference, Milan, Italy, 2007, p. 692.

[19] E.M. Godfrin, S.E. Rodríguez, J.C. Durán, Power subsystem simulation for SAOCOM mission, in: Proceedings of the 26th European Photovoltaic Solar Energy Conference, Hamburg, Germany, 2011, p. 789.

[20] P.T. Houldcroft, Welding Process Technology, Cambridge University Press, New York, 1977.

[21] http://aquarius.nasa.gov/index.html, http://aquarius.nasa.gov/pdfs/overview.pdf.

[22] http://www.conae.gov.ar/prensa/siasge.html.

[23] http://www.ecss.nl/forums/ecss/dispatch.cgi/home/showFile/100439/d20070919074956/No/ecss-e-20-08B-Draft4%2813September2007%29.pdf.

[24] http://www.spenvis.oma.be/.

[25] D.L. King, J.K. Dudley, W.E. Boyson, PVSIM©: A simulation program for photovoltaic cells, modules, and arrays, in: 25th Photovoltaic Specialists Conference, 1996, p. 1295.

[26] J. Plá, M. Barrera, F. Rubinelli, Influence of the InGaP window layer on the optical and electrical performance of GaAs solar cells, Semiconductor Science and Technology 22 (2007) 1122.

[27] J.W. Slemmons, The Microworld of Joining Technology, American Welding Society, New York, 1969.

[28] Solar array design, development, and evaluation for in house spacecraft, Directive No. 563-PG-8700.2.2A, NASA Procedures and Guidelines, 2004, http://standards.gsfc.nasa.gov/gsfc-std/gsfc-std-1000/gsfc-std-1000-b.1.pdf.

[29] E.J. Stofel, E.R. Browne, R.A. Meese, G.J. Vendura, Welded solar cell interconnection, in: 16th Photovoltaic Specialists Conference, San Diego, USA, 1982, pp. 45–50.

[30] H.Y. Tada, J.R. Carter Jr., B.E. Anspaugh, R.G. Downing, Solar Cell Radiation Handbook, JPL Publication 82-69, 1982.

[31] M.J.L. Tamasi, M. Alurralde, I. Prario, A. Filevich, R. Mayer, J.C. Durán, M.G. Martínez Bogado, J. Plá, C.J. Bruno, J. Fernández Vázquez, Comparison of electron and proton radiation damage in solar cells for space uses, in: Proceedings of the 19th European Photovoltaic Solar Energy Conference, Paris, France, 2004, p. 3719.